ACS APPLIED MATERIALS & INTERFACES
Research Article
www.acsami.org

Synthesis of Au−MoS_2 Nanocomposites: Thermal and Friction-Induced Changes to the Structure

T. W. Scharf, R. S. Goeke, P. G. Kotula, and S. V. Prasad*

Materials Science and Engineering Center, Sandia National Laboratories, Albuquerque, New Mexico 87185-0889, United States

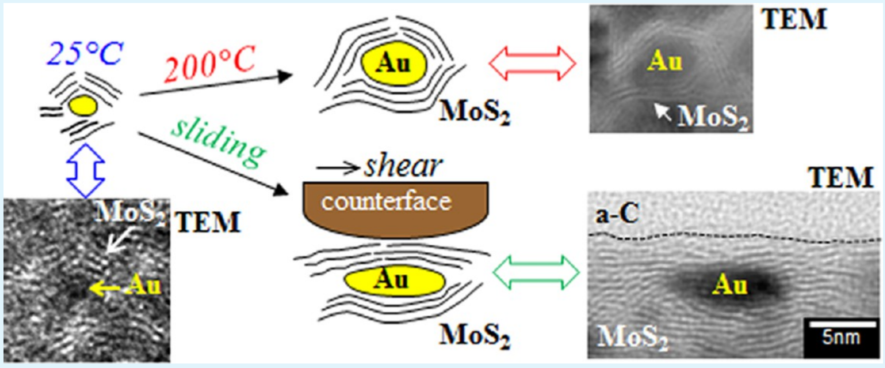

ABSTRACT: The synthesis of Au−MoS_2 nanocomposite thin films and the evolution of their structures during film growth, in situ transmission electron microscopy (TEM) heating, and sliding contact were investigated. TEM revealed that the films deposited at ambient (room) temperature (RT) consisted of 2−4 nm size Au particles in a matrix of MoS_2. With increasing growth temperatures, the nanocomposite film exhibited structural changes: the Au nanoparticles coarsened by diffusion-driven Ostwald ripening to 5−10 nm size and the MoS_2 basal planes encapsulated the Au nanoparticles thereby forming a solid Au-core MoS_2 structure. However, when the RT deposited film was heated inside the TEM, the highly ordered MoS_2 basal planes did not encapsulate the Au, suggesting that MoS_2 surface diffusivity during film growth is different than MoS_2 bulk diffusion. Increases in MoS_2 crystallinity and coarsening of Au nanoparticles (up to 10 nm at 600 °C) were observed during in situ TEM heating of the RT deposited film. Sliding contact during friction and wear tests resulted in a pressure-induced reorientation of MoS_2 basal planes parallel to the sliding direction. The subsurface coarsened Au nanoparticles also provide an underlying load support allowing shear of surface MoS_2 basal planes.

KEYWORDS: *molybdenum disulfide, nanocomposite, friction, in situ heating, Ostwald ripening, transmission electron microscopy*

1. INTRODUCTION

Transition metal dichalcogenides (TMD), for example, MoS_2 and WS_2, are well known for their solid lubricating behavior. This stems from their intermechanical weakness that is intrinsic to their anisotropic bonding and hexagonal (2H) crystal structure, that is, covalent bonding within the S−Mo−S basal planes and weak van der Waals bonds that hold the planes together. During sliding contact, the basal planes slide over one another by intracrystalline slip, which also leads to the formation of smooth transfer films by wear. However, a major obstacle to lubrication by TMD is the presence of unsaturated or dangling bonds on edge planes. If sliding takes place in humid air, such activated surfaces can instantly react with moisture and oxygen in the surrounding environment forming reaction products MoO_3 or WO_3 that result in high friction coefficients (>0.2) and extremely short wear life (typically less than a few thousand cycles because of failure).[1,2] To circumvent the formation of reaction products, there have been studies to synthesize TMD in closed, inert structures. Most notably Tenne, Rapoport, and coworkers[3−5] pioneered the synthesis of hollow inorganic fullerene (IF)−TMD free standing nanoparticles, for example, IF−MoS_2 and IF−WS_2. As a result, the dangling bonds that are responsible for causing oxidation in layered 2H-MoS_2 structures are no longer present in IF-MoS_2 nanoparticles.[6] IF-TMD nanoparticles have also been synthesized to encapsulate solid metal oxide cores, such as MoO_2 nanoparticles (∼35 nm size) encapsulated by MoS_2 layers.[4,7] In addition, IF-TMD nanoparticles have been incorporated into thin films, such as IF-WS_2 in Co[5] and Ni−P[8] metal matrices, as well as hard matrices like TiN.[9] Mechanistic studies revealed dry sliding friction is reduced due to pressure-induced exfoliation and alignment of WS_2 (0002) basal planes parallel to the sliding direction.

TMD-based thin films, in particular MoS_2-based nanocomposites, have been extensively studied for friction and wear reduction in moving mechanical assemblies, especially for space applications.[10−24] The presence of metal dopants can lead to increased film density, hardness, and oxidation resistance

Received: August 16, 2013
Accepted: November 5, 2013
Published: November 5, 2013

dx.doi.org/10.1021/am4034476 | ACS Appl. Mater. Interfaces 2013, 5, 11762−11767

compared to pure MoS_2. While the micro- and macro-tribological behavior of TMD films containing various metal dopants has been well studied, little is known of the structure of these films when synthesized at elevated temperatures, or with post-synthesis heat treatments. For instance, the effects of metal nanoparticle coarsening/coalescence, nanocomposite film densification and crystallinity are not well known, and thus understanding these phenomena and their role in controlling the friction behavior are the focus of this work. Specifically, the thermal behavior during film growth of Au nanoparticles in MoS_2 and the formation of Au-core MoS_2 structures are studied with TEM and in situ TEM heating. Mechanistic studies that unravel how these Au-MoS_2 structures mitigate interfacial shear will also be presented.

2. EXPERIMENTAL METHODS

The films were grown in a custom built sputter co-deposition system that has two 50 mm diameter cathodes (Angstrom Sciences OYNX) located at 90° angles to each other. The rotatable substrate holder is at a 45° angle to each target, so that the deposition flux from both targets arrives simultaneously on the Si (100) substrate at a target to substrate distance of 125 mm. The 50 mm diameter targets were pure MoS_2 and Au (Materion Advanced Chemical) fabricated to >99.999% purity. A radio frequency (RF) power supply was used to deposit from the Au target at a power of ~20 W to enable a lower Au deposition rate. The MoS_2 material was deposited using a pulsed DC power of ~160 W. These power levels were adjusted to achieve a desired composition of ~10 wt.% Au. Pure MoS_2 films were also grown for comparative purposes. The vacuum base pressure was $<5\times10^{-5}$ Pa and Argon was used as the sputter gas with a flow rate of ~50 sccm and working pressure of 0.73 Pa. These conditions resulted in a composite film deposition rate of ~7 Å/s. The films were grown to ~1 μm thickness. The system has the capability to heat the substrate to 400°C, using a backside coil heater.

After deposition, the films were characterized by electron microprobe analysis with wavelength-dispersive X-ray spectroscopy (WDS), dual-beam focused ion beam (FIB) high resolution scanning electron microscopy (HRSEM), and cross-sectional high resolution transmission electron microscopy (HRTEM). The film stoichiometry was characterized with a Cameca SX100 EPMA (Electron Probe MicroAnalyzer). XTEM specimens were prepared with a FEI DB-235 dual-beam FIB/HRSEM and then analyzed in a FEI Tecnai F30-ST TEM/STEM operated at 300 kV. High-angle annular dark field scanning transmission electron microscopy (HAADF-STEM) was also used for Z-contrast imaging. To protect the specimen surfaces from FIB damage and direct Ga ion implantation, the surfaces were first coated with amorphous C (a-C) and then Pt prior to FIB milling. The a-C coating also provided a clear Z-contrast inbetween the surface and Pt. In addition, in situ TEM heating of a FIB prepared RT deposited Au-MoS_2 film was mounted on a Protochips Aduro heater (SiC heating element) and the assembly was inserted into the TEM specimen chamber. This Aduro TEM grid has millisecond thermal ramp times allowing in situ rapid thermal annealing of the film. The imaging resolution and sample stability were better at RT so the film was quickly brought to the desired temperature (up to 600°C), held for 60 seconds and then quenched to RT, allowed to settle, and then re-imaged. The temperature of the specimen is derived from a chip-specific optical pyrometer-derived calibration provided by Protochips and may not reflect the exact temperature the specimen reached in the experiment. Unidirectional sliding friction tests were conducted in open air (~10% RH) for 1000 cycles at a sliding speed of 3.7 mm/s. Either a 1.59 or 3.18 mm diameter Si_3N_4 ball was used as a counterface material at a normal load of 98 or 980 mN, respectively. These values correspond to initial mean Hertzian contact pressures of 0.3 and 1.0 GPa, respectively. A transducer in the load arm measured the tangential load over a track distance of 1.6 mm. The ratio of tangential to normal load is the friction coefficient and at least three tests were performed for each condition. Wear rates, expressed in $mm^3/N{\cdot}m$, were calculated as the wear surface volume of the films divided by the contact load and the total distance traveled by the counterface ball. This calculation is equivalent to dividing the average cross-sectional area of the wear surface (determined by white light interferometer profilometry) by the normal load and by the number of cycles.

3. RESULTS AND DISCUSSION

3.1. Nanostructural Evolution during Film Growth.

Microprobe analysis by WDS confirmed that the co-deposited Au-MoS_2 films were composed of ~10 wt.% Au with a S/Mo ratio of 1.6, which is less than the stoichiometric 2. This indicates sulfur deficient films since the sputter process results in some decomposition of the starting MoS_2 molecule, which is common in sputtering of MoS_2 films. While the films will be referred to as MoS_2, the $MoS_{1.6}$ stoichiometry should be noted. Figure 1 shows cross-sectional HRTEM images of the Au-MoS_2 nanocomposite films deposited at (a) RT and (b) 200°C. The darker features are nanocrystalline Au that coarsened from ~2-4 to ~5-10 nm as the growth temperature increased from RT to 200°C. At lower growth temperatures, such as the RT deposition shown in Figure 1a, the crystalline MoS_2 domain sizes are small (~2 nm) and do not encapsulate/encircle the Au nanoparticles, in contrast to the previously mentioned IF-MoS_2 nanoparticles. However with an increase in growth temperature to 200°C, the surrounding MoS_2 (0002) basal planes shown in Figure 1b begin to encapsulate the Au forming a multi-walled

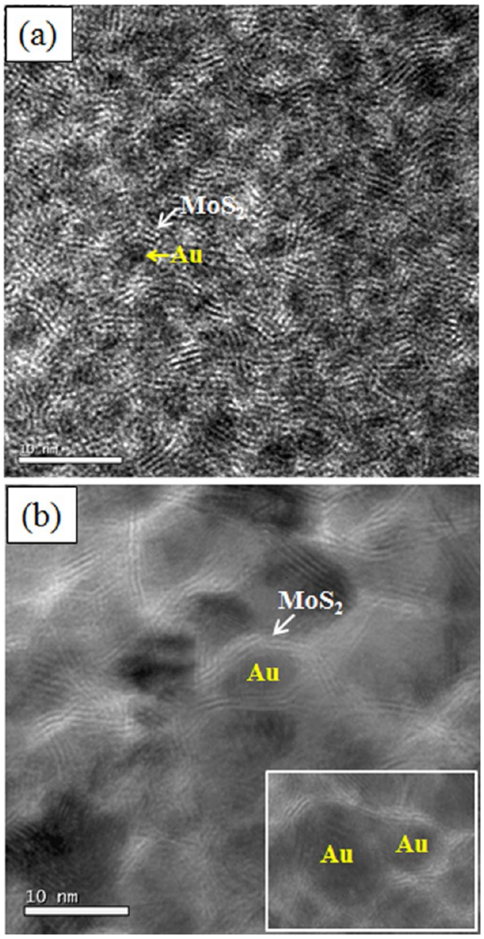

Figure 1. Cross-sectional HRTEM images of the Au-MoS_2 nanocomposite films deposited at (a) RT and (b) 200°C. Inset image in (b) shows coalescence of two Au nanoparticles.

MoS_2 shell, albeit a non-continuous lattice plane shell consisting of several larger MoS_2 domains. It is unlikely that these neighboring domains of MoS_2 basal planes covalently bond to each other and appear to exhibit structural defects such as edge dislocations, although more detailed high resolution TEM studies are needed to elucidate the atomic structure. Figure 1b inset image, acquired from another location along the sample, shows coalescence of two Au nanoparticles with a similar MoS_2-type shell. The formation of these solid Au-core MoS_2 nanostructures are analogous to previous studies on solid core MoO_2 nanoparticles encapsulated by MoS_2 layers, although these were continuous, individual MoS_2 shells.[7] In our study, such nanostructures were only observed in films deposited at substrate temperatures from 200 to 300°C, where the combination of higher temperature, surface diffusivity and kinetic energy from the plasma are believed to be required for their formation. Several structure zone models for thin film growth have been described as a function of growth parameters.[25−27] In these models, the ratio of substrate temperature to the materials melting point (T_s/T_m) is one parameter that can be used to determine the growth mechanism. Zone II ($0.3 < T_s/T_m < 0.5$) is characterized by high surface diffusion of the deposited material leading to granular epitaxial growth.[26] Because the melting point of MoS_2 is ~1185°C, Zone II occurs between 164°C and 456°C. It should be noted that the growth temperature under which long range MoS_2 order was observed in this study is in this Zone II.

Lince et al.[19] reported that higher Au content (≥37 wt.% Au) MoS_2 nanocomposite films results in an amorphous MoS_2 matrix. This indicates that high Au loadings prevented the formation of long range MoS_2 crystallinity in the nanocomposite films. In a similar study on sputtered Ti-WS_2 nanocomposite films grown at 300°C substrate temperature, the higher surface diffusivity and mobility of Ti (5 wt.%) produced crystalline WS_2; however, higher weight percentages of Ti (≥14 wt.%) in the films resulted in amorphous WS_2.[28] In contrast to Au-core MoS_2 nanostructures, WS_2 basal planes were not curved and no Ti nanoparticles were formed suggesting that Ti substitutional solid solution with W may have occurred in the WS_2 lattice during deposition.

3.2. Nanostructural Evolution during in Situ TEM Heating. To determine if these solid Au-core MoS_2 nanostructures could be formed after RT deposition, vacuum annealing of the RT deposited Au-MoS_2 nanocomposite film (Figure 1a) was performed inside the TEM while monitoring thermally-induced changes in situ. The TEM grid heating stage with opening to image the RT deposited Au-MoS_2 film FIB cross-section (~100 nm thick) is shown in Figure 2. The inset in Figure 2 is a higher magnification cross-sectional HAADF-STEM image that shows darker vertical lines in the Au-MoS_2 film indicative of some intercolumnar porosity during growth. Figure 3 shows a sequence of HAADF-STEM images acquired during in situ TEM heating. Below 200°C there were no observable changes to the nanocomposite film structure. From the 200 to 600°C range, several structural changes occur in the film with increasing temperature: the Au nanoparticles (bright spots) coarsen into larger particles and this continues up to 600°C, and the intercolumnar porosity begins to disappear, that is, densification of the film. The yellow arrows in Figure 3 show Au nanoparticles that have coarsened with respect to the previous temperature step.

The series of images in Figure 3 was collected upon cooling from the designated higher temperature to room temperature.

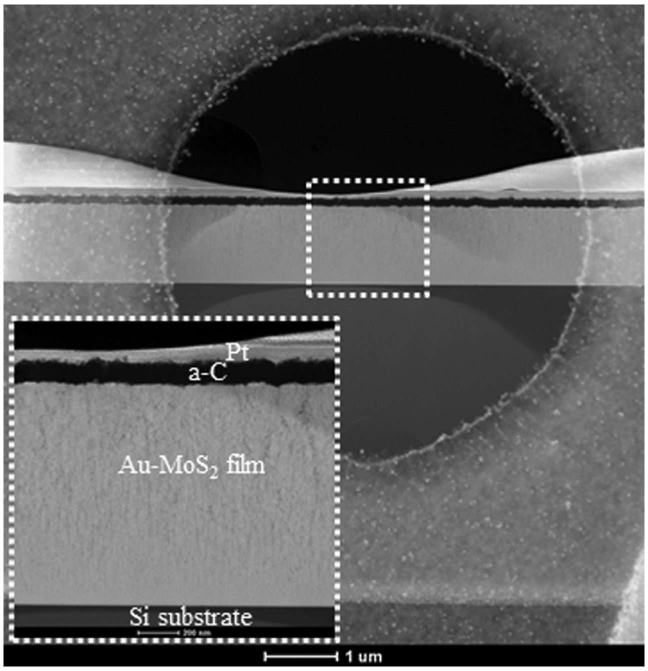

Figure 2. In situ TEM grid heating stage showing FIB cross-section of Au-MoS_2 nanocomposite film deposited at RT over electron transparent opening. Inset box shows higher magnification cross-sectional HAADF-STEM image.

The melting temperature of Au decreases significantly from its bulk value (1064°C) when particle dimensions are reduced to the nanoscale, an ~3 nm diameter Au particle can melt at temperatures as low as 500°C because of the increase in the surface/volume ratio.[29,30] However, the nanoparticle size versus temperature images in Figure 3 show that larger Au nanoparticles grow at the expense of the smaller ones (red arrows in Figure 3) above 400°C in a solid-state, Ostwald ripening process before they reach the size-dependent melting points of isolated Au nanoparticles. Similar in some respects to the present work, Reich et al.[30] studied how native Au nanoparticles with mean diameter of 4 nm found in the mineral arsenian pyrite [$Fe(S,As)_2$], thermally evolved during in situ TEM heating to 650°C. They determined that above 370°C coarsening also occurs by diffusion-driven Ostwald ripening. In addition, Walsh et al.[31] determined with in situ TEM heating that Ostwald ripening of Au nanoparticles becomes the dominant growth process at higher temperatures of 500°C. Similar to Au nanoparticles, in situ TEM heating studies show that Pt nanoparticles can also exhibit Ostwald ripening between 470°C[32] and 650°C.[33] Corresponding HRTEM images of the same nanocomposite film are shown in Figure 4 where the coarsened Au nanoparticles appear darker. These images show more clearly highly crystalline MoS_2 domains especially above 400°C. However, unlike heating during film growth, the highly ordered MoS_2 basal planes did not encapsulate the Au, which suggests that the higher MoS_2 surface diffusivity and kinetic energy from the plasma during film growth are likely responsible for the formation of the Au-core MoS_2 nanostructures. In a related study, amorphous spherical WS_2 and MoS_2 nanoparticles were in situ heated in the TEM and determined to crystallize at higher temperatures of >400°C.[34] The authors also determined that with increasing temperature the size and crystallinity of the MoS_2 layers increased, similar to the structures shown in Figure 4. At temperatures of >500 °C,

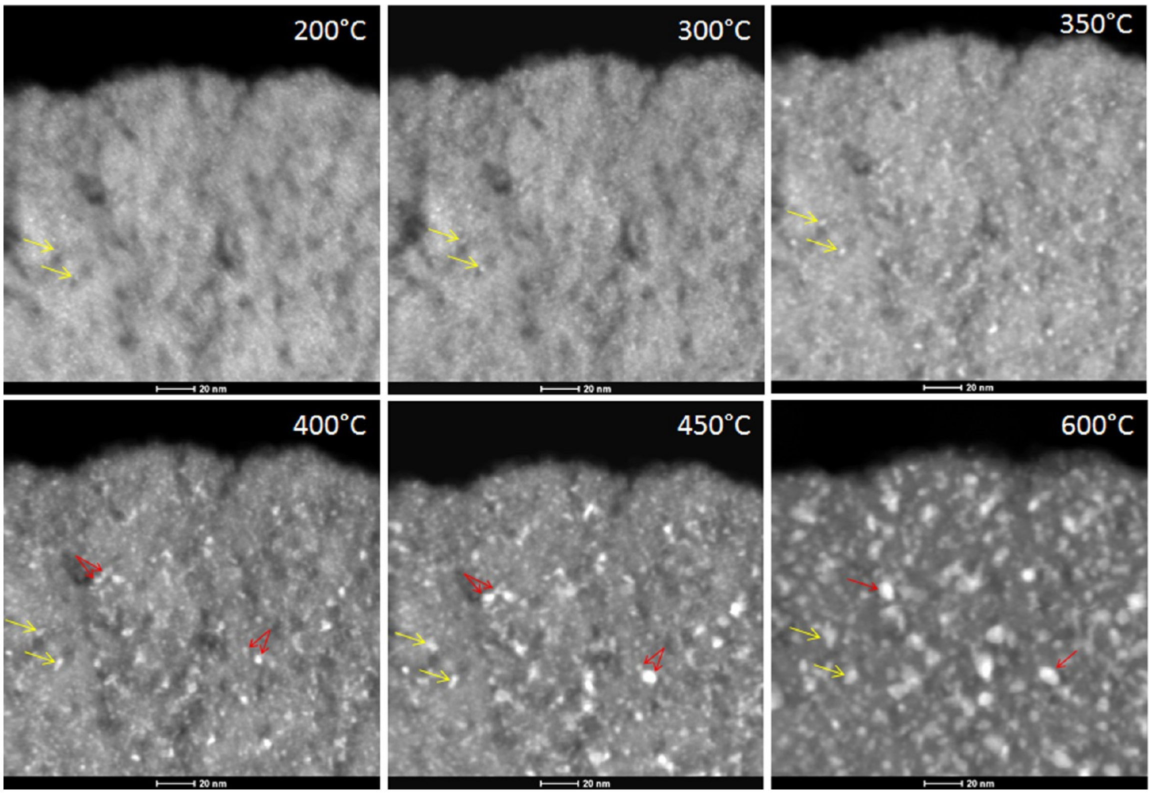

Figure 3. Cross-sectional HAADF-STEM series of images showing Ostwald ripening of Au nanoparticles and MoS_2 nanocomposite film densification with increasing temperature. Yellow arrows show Au nanoparticles that have coarsened with respect to previous temperature step. Red arrows show larger Au nanoparticles that grow at the expense of the smaller ones.

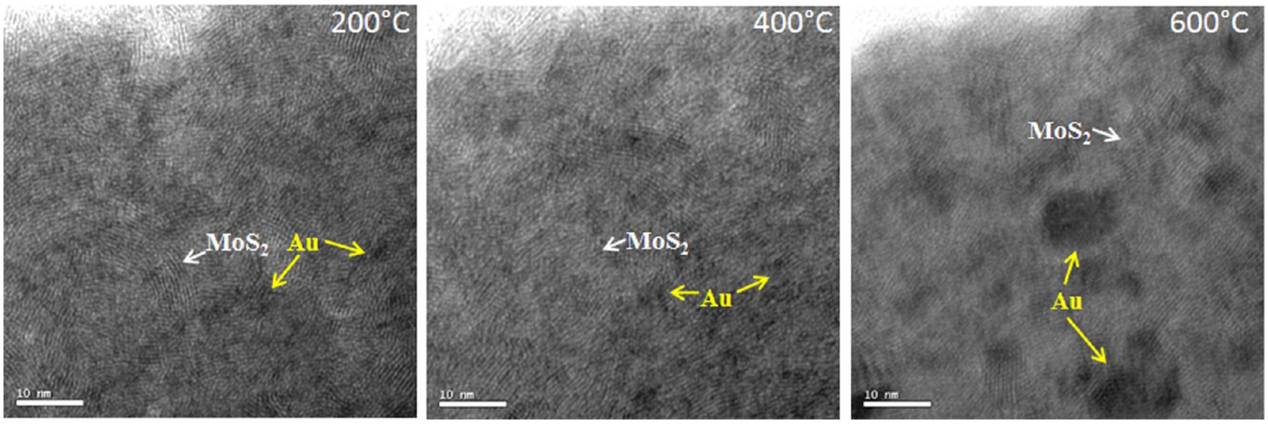

Figure 4. Corresponding cross-sectional HRTEM images of Au coarsening and MoS_2 domain size increasing with temperature. There is no evidence of a closed MoS_2 basal plane shell.

bending of the MoS_2 basal planes started, followed by the formation of closed (onion-like) MoS_2 nanoparticles with a hollow core at temperatures of >700°C. This is in contrast to Figure 4 images that show MoS_2 basal planes do not encapsulate the coarsened Au nanoparticles during in situ TEM heating. Therefore, the Au nanoparticles, as they coarsen with increasing temperature, may be inhibiting MoS_2 from encapsulating them.

3.3. Nanostructural Evolution during Sliding.

Friction coefficients and wear rates of RT deposited Au-MoS_2 nanocomposite (Figure 1a) and pure MoS_2 films under varying contact pressures are listed in Table 1. The Au–MoS_2 nanocomposite film exhibited lower friction at both lower and higher contact pressures compared to the pure MoS_2 film suggesting the Au nanoparticles are playing a role in friction. With increasing contact pressure from 0.3 to 1.0 GPa, the friction coefficient decreased indicating non-Amontonian

Table 1. Steady-State Friction Coefficient and Wear Rate Values for RT Deposited Au–MoS_2 Nanocomposite and Pure MoS_2 Films under Varying Contact Pressures

film	mean hertzian contact pressure (GPa)	steady-state friction coefficients	wear rate (mm^3/N·m)
RT-deposited Au-MoS_2 nanocomposite	0.3	0.12 ± 0.02	$3 \pm 1 \times 10^{-6}$
	1.0	0.05 ± 0.008	
pure MoS_2	0.65	0.25 ± 0.09	$6 \pm 1.5 \times 10^{-5}$

behavior, similar to previous reports on MoS_2-based materials.[19,20,22,35,36] The friction coefficient of 0.05 under the 1.0 GPa contact pressure is a very low value for MoS_2-based films in humid air. In examining the wear track after sliding, the pure MoS_2 film had areas where the film wore away to the base Si substrate explaining the high and large deviations in the friction coefficient values. Where there was film still present in the track, the wear rate was calculated to be 6×10^{-5} $mm^3/N{\cdot}m$. In contrast, the nanocomposite film had a significantly lower wear rate of 3×10^{-6} $mm^3/N{\cdot}m$ under both contact pressures with no evidence of film depletion in either wear tracks.

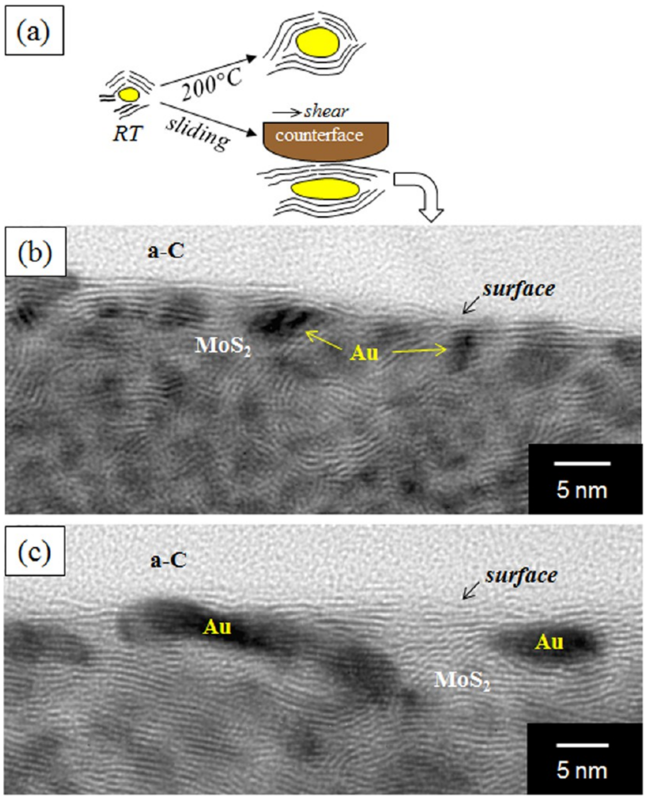

Figure 5. (a) Schematic representations of nanostructural evolution during 200°C film growth (Figure 1b) and sliding on RT deposited Au-MoS_2 nanocomposite film: thermally-induced increase in surface MoS_2 crystallinity, Au coarsening, and, in the case of sliding, a shear-induced reorientation of MoS_2 (0002) basal planes parallel to the sliding direction to achieve low friction. Corresponding cross-sectional HRTEM images taken inside the wear track of RT deposited Au-MoS_2 nanocomposite film at (b) 0.3 and (c) 1.0 GPa contact pressures showing the sliding-induced structural evolution of several Au-MoS_2 nanostructures.

Figure 5a shows schematics of the nanostructural evolution during 200°C film growth and sliding contact on the RT deposited Au-MoS_2 nanocomposite film (Figure 1a). There are three main phenomena that occur during sliding as revealed by the cross-sectional TEM images in Figure 5b and 5c: (1) shear-induced reorientation of surface MoS_2 (0002) basal planes parallel to the sliding direction, (2) increase in surface and subsurface MoS_2 domain size and crystallinity, and (3) coarsening of the near surface Au nanoparticles. In the case of the latter two, the 200°C deposited film, previously shown in Figure 1b, also exhibited this structural evolution. During sliding, these phenomena are more pronounced, especially when the contact pressure increases from 0.3 (Figure 5b) to 1.0 GPa (Figure 5c). Both thermal and mechanical (tribological) stresses can be operative during sliding and decoupling their effects is difficult. In the case of the former, high contact pressure, sliding speed and friction coefficients all contribute to increasing the interfacial flash temperature in sliding contacts. In this study, all of these values are relatively low with the only variable being the change in contact pressure. As shown in Figure 5b and 5c, the increase in contact pressure resulted in the aforementioned changes in structure. It was previously shown in Figures 1 and 4 that increasing the temperature resulted in increases in MoS_2 domain size and crystallinity and Au nanoparticle coarsening, similar to what is occurring during sliding shown in Figure 5. Therefore, there is likely a near surface thermal component to friction, while the reorientation of MoS_2 (0002) basal planes parallel to the sliding direction is more likely to be shear-induced. Thus, the increase in contact pressure would result in both a thermally-induced increase in surface MoS_2 domain size/crystallinity and Au coarsening as well as sliding (shear)-induced reorientation of the MoS_2 (0002) planes parallel to the sliding direction and elongation of Au nanoparticles at the higher contact stress (Figure 5c).

These nanostructural changes in MoS_2 and Au are responsible for the lowering of the friction coefficient from ~0.12 to ~0.05 as mean contact pressure changes from 0.3 to 1 GPa. Lowering of the friction coefficient with increasing contact pressure (or normal load) is well known for many solid lubricant films like MoS_2, according to the Bowden and Tabor analysis for Hertzian contacts where friction coefficient is proportional to $(\text{normal load})^{-1/3}$.[24,37] The reorientation of the MoS_2 (0002) planes under both contact pressures resulted in lowering of the interfacial shear stress because this texture is conducive to easy shear providing a thin blanket (~5 basal planes) of solid lubrication. In addition, the sliding-induced deformation of the Au-MoS_2 nanostructures results in elongation of the near surface Au nanoparticles along the sliding direction shown in Figure 5. While it is known that exfoliation of basal planes in IF-MoS_2 nanoparticles is responsible for low friction,[5,8,38−43] this study shows that nanocomposite films can also exhibit a similar mechanism where the increase in coarsened Au nanoparticles at higher contact pressures act as an underlying load bearing material supporting shear of surface MoS_2 (0002) basal planes during interfacial sliding. This coarsened (and likely hardened) underlying load bearing material in principle could reduce the contact area during sliding, which would result in decreased friction in comparison to the pure MoS_2 film according to the Bowden-Tabor concept.[37] In addition to exfoliation of basal planes, rolling has also been observed in free-standing IF nanoparticles,[41,42] particularly at lower contact pressures, for example, <100 MPa.[42] While difficult to prove, there was no direct evidence of Au nanoparticle/MoS_2 rolling during interfacial sliding. Also, rolling would be very difficult since the Au-core MoS_2 structures are confined within the film, that is, they are not free-standing. Lastly, the mating sliding surface of the Si_3N_4 counterface contained a transfer film (tribofilm). It is well known that sliding on TMD thin films results in transfer films adhering to the counterface resulting in interfacial sliding between the wear track and transfer film. While the transfer film was not thoroughly characterized, the authors have previously reported for similar $MoS_2/Sb_2O_3/Au$ nanocomposite films that MoS_2 (0002) basal planes on the surface of the transfer film also align parallel to the sliding direction resulting in a self-mated MoS_2/MoS_2 interface.[22]

4. CONCLUSIONS

Au-MoS_2 nanocomposite films were synthesized by co-sputtering from Au and MoS_2 targets. At higher growth temperatures, solid Au-core MoS_2 nanostructures were formed due to a combination of high surface diffusivity and kinetic energy from the plasma. TEM studies on the RT deposited film with in situ heating showed that there was coarsening of Au nanoparticles governed by the Ostwald ripening mechanism and nanocomposite film densification with an increase in MoS_2 crystallinity. Coarsened Au-MoS_2 nanostructures also form in sliding contacts where there is both a thermally-induced increase in surface MoS_2 domain size and crystallinity and a pressure-induced reorientation of MoS_2 basal planes parallel to the sliding direction that are both responsible for lowering of friction. While it is known that exfoliation of IF-MoS_2 nanoparticles is responsible for low friction, we show here that nanocomposite films can also exhibit a similar mechanism where the coarsened Au nanoparticles act as an underlying load bearing material supporting the parallel MoS_2 (0002) basal planes during interfacial sliding.

■ AUTHOR INFORMATION

Notes

The authors declare no competing financial interest.

T. W. Scharf is on faculty sabbatical from the Department of Materials Science and Engineering, The University of North Texas, Denton, TX 76203-5310, USA

■ ACKNOWLEDGMENTS

Sandia National Laboratories is a multiprogram laboratory managed and operated by Sandia Corporation, a wholly owned subsidiary of Lockheed Martin Corporation, for the U.S. Department of Energy's National Nuclear Security Administration under Contract DE-AC04-94AL85000. The authors would like to acknowledge Nic Argibay for critical review. We also thank Cathy Sobczak for co-sputtering the films, Garry Bryant for preparing FIB samples, and Richard Grant for electron microprobe analysis.

■ REFERENCES

(1) Sliney, H.E. *Tribol. Inter.* **1982**, *15*, 303−314.

(2) Prasad, S.V.; Zabinski, J.S. *J. Mater. Sci. Lett.* **1993**, *12*, 1413−1415.

(3) Tenne, R.; Margulis, L.; Genut, M.; Hodes, G. *Nature* **1992**, *360*, 444−446.

(4) Cizaire, L.; Vacher, B.; LeMogne, T.; Martin, J.M.; Rapoport, L.; Margolin, A.; Tenne, R. *Surf. Coat. Technol.* **2002**, *160*, 282−287.

(5) Friedman, H.; Eidelman, O.; Feldman, Y.; Moshkovich, A.; Perfiliev, V.; Rapoport, L.; Cohen, H.; Yoffe, A.; Tenne, R. *Nanotechnology* **2007**, *18*, 115703.

(6) Prasad, S.V.; Zabinski, J.S. *Nature* **1997**, *387*, 761−763.

(7) Frey, G.L.; Elani, S.; Homyonfer, M.; Feldman, Y.; Tenne, R. *Phys. Rev. B* **1998**, *57*, 6666−6671.

(8) André, B.; Gustavsson, F.; Svahn, F.; Jacobson, S. *Surf. Coat. Technol.* **2012**, *206*, 2325−2329.

(9) Polcar, T.; Mohan, D.B.; Sandu, C.S.; Radnoczi, G.; Cavaleiro, A. *Thin Solid Films* **2011**, *519*, 3191−3195.

(10) Spalvins, T. *Thin Solid Films* **1984**, *118*, 375−384.

(11) Hilton, M.R.; Fleischauer, P.D. *Surf. Coat. Technol.* **1992**, *54-55*, 435−442.

(12) Wahl, K.J.; Seitzman, L.E.; Bolster, R.N.; Singer, I.L. *Surf. Coat. Technol.* **1995**, *73*, 152−159.

(13) Zabinski, J.S.; Donley, M.S.; Walck, S.D.; Schneider, T.R.; McDevitt, N.T. *Tribol. Trans.* **1995**, *38*, 894−904.

(14) Renevier, N.M.; Fox, V.C.; Teer, D.G.; Hampshire, J. *Surf. Coat. Technol.* **2000**, *127*, 24−37.

(15) Savan, A.; Simmonds, M.C.; Huang, Y.; Constable, C.P.; Creasey, S.; Gerbig, Y.; Haefke, H.; Lewis, D.B. *Thin Solid Films* **2005**, *489*, 137−144.

(16) Zabinski, J.S.; Bultman, J.E.; Sanders, J.H.; Hu, J.J. *Tribol. Lett.* **2006**, *23*, 155−163.

(17) Chromik, R.R.; Baker, C.C.; Voevodin, A.A.; Wahl, K.J. *Wear* **2007**, *262*, 1239−1252.

(18) Hamilton, M.A.; Alvarez, L.A.; Mauntler, N.A.; Argibay, N.; Colbert, R.; Burris, D.L.; Muratore, C.; Voevodin, A.A.; Perry, S.S.; Sawyer, W.G. *Tribol. Lett.* **2008**, *32*, 91−98.

(19) Lince, J.R.; Kim, H.I.; Adams, P.M.; Dickrell, D.J.; Dugger, M.T. *Thin Solid Films* **2009**, *517*, 5516−5522.

(20) Muratore, C.; Voevodin, A.A. *Annu. Rev. Mater. Res.* **2009**, *39*, 297−324.

(21) Stoyanov, P.; Chromik, R.R.; Goldbaum, D.; Lince, J.R.; Zhang, X. *Tribol. Lett.* **2010**, *40*, 199−211.

(22) Scharf, T.W.; Kotula, P.G.; Prasad, S.V. *Acta Mater.* **2010**, *58*, 4100−4109.

(23) Prasad, S.V.; Renk, T.J.; Kotula, P.G.; DebRoy, T. *Mater. Lett.* **2011**, *65*, 4−6.

(24) Scharf, T.W.; Prasad, S.V. *J. Mater. Sci.* **2013**, *48*, 511−531.

(25) Thornton, J.A. *J. Vac. Sci. Technol.* **1974**, *11*, 666−670.

(26) Hentzell, H. T. G.; Grovenor, C. R. M.; Smith, D. A. *J. Vac. Sci. Technol. A* **1984**, *2*, 218−219.

(27) Barna, P.B.; Adamik, M. *Thin Solid Films* **1998**, *317*, 27−33.

(28) Scharf, T.W.; Rajendran, A.; Banerjee, R.; Sequeda, F. *Thin Solid Films* **2009**, *517*, 5666−5675.

(29) Buffat, P.; Borel, J.P. *Phys. Rev. A* **1976**, *13*, 2287−2298.

(30) Reich, M.; Utsunomiya, S.; Kesler, S.E.; Wang, L.; Ewing, R.C.; Becker, U. *Geology* **2006**, *34*, 1033−1036.

(31) Walsh, M.J.; Yoshida, K.; Gai, P.L.; Boyes, E.D. *J. Phys. Conf. Ser.* **2010**, *241*, No. 012058.

(32) Prestat, E.; Popescu, R.; Blank, H.; Schneider, R.; Gerthsen, D. *Surf. Sci.* **2013**, *609*, 195−202.

(33) Simonsen, S.B.; Chorkendorff, I.; Dahl, S.; Skoglundh, M.; Sehested, J.; Helveg, S. *J. Catal.* **2011**, *281*, 147−155.

(34) Zink, N.; Therese, H.A.; Pansiot, J.; Yella, A.; Banhart, F.; Tremel, W. *Chem. Mater.* **2008**, *20*, 65−71.

(35) Lince, J.R. *Tribol. Lett.* **2004**, *17*, 419−428.

(36) Stoyanov, P.; Fishman, J.Z.; Lince, J.R.; Chromik, R.R. *Surf. Coat. Technol.* **2008**, *203*, 761−765.

(37) Bowden, F.P.; Tabor, D. *The Friction and Lubrication of Solids*; Clarendon Press: Oxford, U.K., 1986; pp 112−120.

(38) Chhowalla, M.; Amaratunga, G. A. J. *Nature* **2000**, *407*, 164−167.

(39) Rosentsveig, R.; Margolin, A.; Gorodnev, A.; Popovitz-Biro, R.; Feldman, Y.; Rapoport, L.; Novema, Y.; Naveh, G.; Tenne, R. *J. Mater. Chem.* **2009**, *19*, 4368−4374.

(40) Joly-Pottuz, L.; Martin, J.M.; Dassenoy, F.; Belin, M.; Montagnac, R.; Reynard, B. *J. Appl. Phys.* **2006**, *99*, 023524−023528.

(41) Tevet, O.; Von-Huth, P.; Popovitz-Biro, R.; Rosentsveig, R.; Wagner, D.H.; Tenne, R. *Proc. Natl Acad. Sci.* **2011**, *108*, 19901−19906.

(42) Lahouij, I.; Dassenoy, F.; Vacher, B.; Martin, J. M. *Tribol. Lett.* **2012**, *45*, 131−141.

(43) Lahouij, I.; Bucholz, E.W.; Vacher, B.; Sinnott, S.B.; Martin, J.M.; Dassenoy, F. *Nanotechnology* **2012**, *23*, No. 375701.